Turbulent transport and entrainment in jets and plumes: a DNS study

Maarten van Reeuwijk,[1] Pietro Salizzoni,[2] Gary R. Hunt,[3] and John Craske[1]
[1)] *Department of Civil and Environmental Engineering, Imperial College London, London SW7 2AZ, UK*
[2)] *Laboratoire de Mécanique des Fluides et d'Acoustique, University of Lyon, CNRS UMR 5509 Ecole Centrale de Lyon, INSA Lyon, Université Claude Bernard, 36, avenue Guy de Collongue, 69134 Ecully, France*
[3)] *Department of Engineering, University of Cambridge, Cambridge CB2 1PZ, UK*

(Dated: 26 July 2016)

We present a new DNS data set for a statistically axisymmetric turbulent jet, plume and forced plume in a domain of size $40r_0 \times 40r_0 \times 60r_0$, where r_0 is the source diameter. The data set supports the validity of the Priestley and Ball entrainment model in unstratified environments (excluding the region near the source), which is corroborated further by the Wang and Law and Ezzamel *et al.* experimental data sets, the latter being corrected for a small but influential co-flow that affected the statistics. We show that the second-order turbulence statistics in the core region of the jet and the plume are practically indistinguishable, although there are significant differences near the plume edge. The DNS data indicates that the turbulent Prandtl number is about 0.7 for both jets and plumes. For plumes, this value is a result of the difference in the ratio of the radial turbulent transport of radial momentum and buoyancy. For jets however, the value originates from a different spread of the buoyancy and velocity profiles, in spite of the fact that the ratio of radial turbulent transport terms is approximately unity. The DNS data does not show any evidence of similarity drift associated with gradual variations in the ratio of buoyancy profile to velocity profile widths.

I. INTRODUCTION

The mixing of buoyant fluid releases with the surrounding fluid is of primary concern for a wide number of industrial and environmental turbulent flows, spanning the ascending motions of thermals in the atmosphere, the rise and fall of volcanic eruption columns, the release of airborne pollutants or the propagation of smoke in free or enclosed spaces[1]. Much attention has therefore been paid to the turbulence dynamics of buoyant releases in a multiplicity of flow configurations. One of the most studied flows among these, commonly referred to as a 'plume', is the free-shear flow arising from a localised source of buoyancy. Since the pioneering work of Zel'dovich[2], Priestley and Ball[3] and Morton, Taylor, and Turner[4], plumes have been the object of several theoretical[5], experimental[6–9] and numerical[10,11] investigations and are well documented in a number of review articles[12–14]. In this context, the well-known turbulent jet can be regarded as a plume without buoyancy and provides a reference state for understanding how buoyancy modifies the behaviour of these free-shear flows.

Jets and plumes are canonical examples of flows that evolve in a self-similar fashion[14]: sufficiently far from the source, a rescaling of the radial coordinate and dependent variables by a characteristic local width r_m, velocity w_m and buoyancy b_m, results in a collapse of the data onto a single curve. The velocity and buoyancy profiles are well represented by a Gaussian form[12], and self-similarity allows power laws, relating the scales r_m, w_m and b_m to the streamwise (vertical direction opposing the gravitational vector) z-coordinate[4], to be deduced. Due to the presence of buoyancy, the z-dependence of plumes is markedly different to that of jets, yet in other respects, as discussed in this paper, these flows are broadly alike.

There are several ways to determine the characteristic scales r_m, w_m and b_m. A popular experimental method is to capitalise on the Gaussian shape of the velocity and buoyancy profiles, and associate r_m with the standard deviation of the Gaussian, and w_m and b_m with the maximum velocity and buoyancy, respectively. A method that does not rely directly on the assumption of a Gaussian shape is to determine local scales based on integral quantities of the flow:

$$r_m \equiv \frac{Q}{M^{1/2}}, \quad w_m \equiv \frac{M}{Q}, \quad b_m \equiv \frac{B}{r_m^2}, \tag{1}$$

where the integral volume flux Q, specific momentum flux M and buoyancy B are defined as

$$Q \equiv 2\int_0^\infty \overline{w} r \mathrm{d}r, \quad M \equiv 2\int_0^\infty \overline{w}^2 r \mathrm{d}r, \quad B \equiv 2\int_0^\infty \overline{b} r \mathrm{d}r. \tag{2}$$

Here $\overline{w}$ is the average (ensemble or time) streamwise velocity, $b = g(\rho_e - \rho)/\rho_e$ is the fluid buoyancy and $\overline{b}$ its average value, g is the modulus of the gravitational acceleration and ρ_e the density of the environment. Here, Q, M and B are scaled, rather than actual, integral fluxes due to a factor π that is not present in their definitions; this is common practice as it simplifies the resulting analytical expressions[15].

It should be noted that the definition of b_m, in (1)-(2), is non-standard as it is usually expressed in terms of the buoyancy flux

$$F \equiv 2\int_0^\infty \overline{w}\overline{b}r\mathrm{d}r, \tag{3}$$

as $b_m = F/Q = F/(w_m r_m^2)$. Whilst this is a perfectly reasonable definition, it implicitly assumes averaging over a radius associated with the buoyancy profile which, in general, will not be exactly equal to r_m. With a single lengthscale r_m as defined in (1), it follows that $F = \theta_m w_m r_m^2 b_m$ where θ_m is a dimensionless profile coefficient (see also section III C); thus the definition of b_m in terms of F, in the current framework, is $b_m = F/(\theta_m Q)$. The profile coefficient θ_m is intimately related to the ratio of the widths of the buoyancy and velocity profiles (see section III C), plays an important role in longitudinal mixing in jets[16] and is purportedly responsible for the large scatter in measurements of plume entrainment[17].

The dilution of jets and plumes can be quantified by integrating the continuity equation over the radial direction, which results in

$$\frac{1}{r_m}\frac{\mathrm{d}Q}{\mathrm{d}\zeta} = -2\left[ru\right]_\infty. \tag{4}$$

Here $\zeta \equiv \int_0^z r_m^{-1}\mathrm{d}z'$ is a dimensionless vertical coordinate and $\left[ru\right]_\infty$ is a net volume flux into the jet/plume per unit height. The entrainment assumption[4,18–20], links the radial volume flux to internal jet/plume properties via

$$-\left[ru\right]_\infty = \alpha r_m w_m, \tag{5}$$

where α is the entrainment coefficient. Substitution of (5) into (4) and rearranging results in

$$\alpha = \frac{1}{2Q}\frac{\mathrm{d}Q}{\mathrm{d}\zeta}. \tag{6}$$

Thus, the entrainment coefficient can be interpreted as (half) the relative increase in volume flux over a typical jet/plume radius r_m. This relation also clearly establishes that α is a measure of dilution: the higher its value, the more fluid will be mixed into the jet/plume per (vertical) unit r_m.

Typical ranges of values for α in jets and plumes are, respectively[21], $0.065 < \alpha_j < 0.084$ and $0.10 < \alpha_p < 0.16$, which, in spite of the scatter, strongly suggests that $\alpha_p > \alpha_j$. Using the observation that the spreading rates $\mathrm{d}r_m/\mathrm{d}z$ of jets and plumes are approximately equal[12,22], and the well-known far-field solutions $r_m = 2\alpha_j z$ and $r_m = \frac{6}{5}\alpha_p z$ for jets[23] and plumes[4], respectively, it follows directly that

$$\alpha_p \approx \frac{5}{3}\alpha_j. \tag{7}$$

By applying the relation above to the observed range of values of α_j, we obtain $0.108 < 5\alpha_j/3 < 0.133$, which is in reasonably good agreement with the available data for α_p.

The fact that the spreading rates of jets and plumes are practically identical is intimately linked with the turbulence production in the interior. Indeed, by considering balance equations for the kinetic energy of the mean flow in jets and plumes[17,24–26], the spreading rate can be directly linked to the turbulence production inside the plume. For a self-similar Gaussian plume, ignoring turbulence and pressure effects and assuming $\theta_m = 1$, it follows that[26]

$$\frac{\mathrm{d}r_m}{\mathrm{d}z} = -\frac{3}{4}\delta_m, \tag{8}$$

where

$$\delta_m = \frac{4}{w_m^3 r_m}\int_0^\infty \overline{u'w'}\frac{\mathrm{d}\overline{w}}{\mathrm{d}r}r\mathrm{d}r \tag{9}$$

is a dimensionless profile coefficient associated with the integral of turbulence production due to shear. This quantity is generally negative as it signifies the energy transfer from the mean to the turbulence. Hence, under the realistic assumptions leading to (8), it follows that δ_m is solely responsible for the plume spread, and identical spreading rates imply identical values for δ_m. Direct estimations, either using flow measurements or with high-fidelity simulations, confirm that the value of δ_m for jets and plumes is indeed nearly identical[26].

Using the equation for mean kinetic energy, it is possible to derive entrainment relations that fundamentally link α to the production of turbulence kinetic energy, the Richardson number and shape effects. For a self-similar Gaussian plume with $\theta_m = 1$, ignoring turbulence and pressure effects[24], the entrainment relation is[26]

$$\alpha = -\frac{3}{8}\delta_m + \frac{1}{4}\mathrm{Ri}, \tag{10}$$

where the Richardson number Ri, defined as

$$\mathrm{Ri} = \frac{b_m r_m}{w_m^2} = \frac{BQ}{M^{3/2}} \tag{11}$$

characterises the significance of buoyancy compared with inertia. An important implication of the fact that δ_m does not differ between jets and plumes (i.e. is constant) is that (10) shows that the difference in α is caused purely by the influence of mean buoyancy via Ri. By using the observation that δ_m is a constant, (10) can be rewritten as[26]

$$\alpha = \alpha_j + (\alpha_p - \alpha_j)\Gamma \tag{12}$$

which is commonly referred to as the Priestley and Ball entrainment model[3,24]. Here, $\Gamma = \mathrm{Ri}/\mathrm{Ri}_p$ is the flux balance parameter, where $\mathrm{Ri}_p = 8\alpha_p\beta_g/5$ is the Richardson number for a pure plume[26] and β_g is a profile coefficient associated with the total momentum flux (see section III C for its definition). The condition $\Gamma = 1$ represents a stable equilibrium (with respect to perturbations in Γ), a condition referred to as that of a 'pure plume'. The other equilibrium condition is given by $\Gamma = 0$, i.e. that of a 'pure jet', a condition which is however unstable to the addition of an arbitrarily small amount of buoyancy[15]. For forced plumes, which have an excess of momentum (relative to pure plume conditions) at the source[5], $0 < \Gamma < 1$, whereas $\Gamma > 1$ for lazy plumes, which have a deficit of momentum[15]. Previous experimental studies observed that (12) accurately describes the behaviour of jets, plumes and forced plumes[9,25].

If the magnitude of the dimensionless turbulence production δ_m is approximately equal in jets and plumes, one is led to ask what this implies about the radial transport of scalar quantities in the flow. The turbulent Prandtl number

$$\mathrm{Pr}_T = \frac{\nu_T}{D_T}, \tag{13}$$

where ν_T and D_T are the eddy viscosity and eddy diffusivity, respectively, quantifies the effectiveness with which the flow mixes momentum compared with buoyancy/mass and is a useful quantity in this regard. The consensus is that $\mathrm{Pr}_T = 0.7$ in axisymmetric jets and plumes[27], which suggests that turbulence transports buoyancy/mass more efficiently than momentum[28] in both cases. However, the underlying physics and their implications for entrainment and for the relative widths of the scalar profile compared with the velocity profile are not understood. For jets there is a good agreement between investigators that suggests the scalar field is wider than the velocity field[6,9,23,27]. For plumes however, as discussed in[29] and elsewhere, there is significant uncertainty: some studies reveal that the velocity field is wider than the buoyancy field[8,27,30], others reveal that it is narrower[6,23,25,31]; several results imply that the velocity and scalar profiles have roughly the same width[9,32] and some imply that the relative width varies with height[17]. The present paper seeks to untangle the confusion regarding the relationship between Pr_T and the widths of the scalar and velocity profiles by supplementing the available experimental data with precise information from direct numerical simulation (DNS).

Herein, we follow the approach of Ezzamel, Salizzoni, and Hunt [25] by performing a side-by-side comparison of turbulent jets, plumes and the intermediate case of a forced plume, but using DNS rather than laboratory experiments. With DNS it is relatively straightforward to prescribe boundary conditions consistent with the analytical solutions and furthermore, DNS provides access to all variables, including pressure, at

Kolmogorov-scale resolutions. In section II, the simulation details are presented. Integral flow statistics, such as the evolution of $\Gamma(z)$, are presented in section III A and the deduced entrainment coefficient α is shown to follow closely the Priestley and Ball entrainment model (12). Self-similarity of the first- and second-order statistics is discussed in section III B, which includes an analysis of the invariants of the anisotropy tensor. Profile coefficients, which represent the relative contribution of various physical processes relative to the characteristic scales are presented in section III C, and these are used to decompose the entrainment coefficient into its individual components in section III D. Section III E discusses the radial turbulent transport of streamwise momentum and buoyancy, as quantified by the eddy viscosity ν_T and diffusivity D_T. The turbulent Prandtl number will be decomposed and it is shown that even though jets and plumes share a very similar value for Pr_T, the underlying reason in each case is different. Concluding remarks are made in section IV.

II. SIMULATION DETAILS

We simulate axisymmetric jets and plumes driven by an isolated source of steady specific momentum flux M_0, volume flux Q_0 and buoyancy flux F_0. The source is approximately circular and located at the centre of the base of a cuboidal domain of size $40^2 \times 60$ source radii, r_0. The fluid motion is governed by the incompressible Navier-Stokes equations under the Boussinesq approximation, which we solve numerically using $1280^2 \times 1920$ computational cells over a uniform Cartesian grid. The code for the DNS employs a spatial discretisation of fourth-order accuracy that conserves volume, momentum and energy, and integration in time is performed using a third-order Adams Bashforth scheme[33]. On the vertical and top faces of the domain we impose open boundary conditions. These allow fluid to enter and leave the domain in a manner that is consistent with flow in an unconfined domain[34]. We initiate the turbulence by applying uncorrelated perturbations of 1% to the velocities in the first cell above the source.

To simulate the jet J we impose a constant uniform vertical velocity w_0 at the source. Consequently, a constant scalar flux can be maintained by imposing a Dirichlet boundary condition $b = b_0$ on a given scalar quantity b at the source. For the jet simulation J, this scalar quantity is passive, i.e. its presence does not imply a source term in the momentum equation. In the forced plume simulation F, for which b corresponds to buoyancy, the Dirichlet boundary condition on b at the source results in a positive buoyancy flux F_0. The source conditions used in the simulation of plume P correspond to $w_0 = 0$ and a specified positive integral buoyancy flux F_0; in practice, the buoyancy flux F_0 is a diffusive flux resulting from a Neumann condition on the buoyancy at the source. Therefore, the plume simulation P is infinitely lazy at the source ($\Gamma_0 \equiv 5F_0Q_0^2/(8\alpha_p M_0^{5/2}) = \infty$) although, over a relatively short distance, plume P becomes pure. Based on the analysis of Hunt and Kaye [15], in which a constant entrainment coefficient model is assumed, the rate of decrease of the local Richardson number immediately above a highly-lazy plume source scales as

$$\left.\frac{d\Gamma}{d\zeta}\right|_{\zeta=0} \propto -\Gamma_0^{9/5}. \tag{14}$$

Thus, the vertical distance required to approach pure-plume behaviour reduces to zero as the laziness of the source increases, i.e. as $\Gamma_0 \to \infty$. As a consequence, our plume arising from the heated disc boundary condition, which represents the limit of an infinitely lazy plume source, is expected to establish pure-plume behaviour immediately above the source and, as such, to closely mimic a true pure-plume source. For jet J and forced plume F we define the source Reynolds number $\mathrm{Re}_0 \equiv 2M_0^{1/2}/\nu$ and for plume P, $\mathrm{Re}_0 \equiv 2F_0^{1/3}r_0^{2/3}/\nu$. The calculated values of Re_0, in addition to further details of the simulations, can be found in Table I.

Statistics were acquired from each simulation over a duration that is large in comparison with the typical turnover time. For jet J and forced plume F, the turnover time based on the source conditions is $\tau_0 \equiv r_0^2/M_0^{1/2}$. For plume P, $\tau_0 \equiv r_0^{4/3}/F_0^{1/3}$. Prior to obtaining statistics we ensure that transient effects arising from initial conditions are imperceptible in the leading-order statistics. Statistics were gathered over the time-period shown in Table I.

Azimuthally averaged data was obtained by partitioning the domain into concentric cylindrical cells and averaging over all cells lying within a given shell. To compute integrals over lateral slices of the jet (for the definition of these integrals see section III C), we define the upper limit of integration r_d according to $\overline{w}(r_d, z, t) = 0.02\,\overline{w}(0, z, t)$.

Detailed validation of the jet and plume simulations was performed in previous work[35,36] for simulations at identical Re_0. The results presented below are for a larger domain and are obtained with even higher

	$N_xN_yN_z$	$L_xL_yL_z/r_0$	Re_0	Γ_0	t_{run}/τ_0	α	z_v/r_0	a_w	a_b	$\langle \mathrm{Pr}_T \rangle$
J	$1280^2 \times 1920$	$40^2 \times 60$	5000	0	400	0.067	-3.66	0.12	0.14	0.72
F	$1280^2 \times 1920$	$40^2 \times 60$	5000	≈ 0.03	480	varies	varies			
P	$1280^2 \times 1920$	$40^2 \times 60$	1667	∞	480	0.105	-3.90	0.13	0.15	0.68

TABLE I. Simulation details. The entrainment coefficient α and virtual origin z_v are determined directly from r_m (see Fig. 1). The constants a_w and a_b are prefactors of the mixing lengths of velocity and buoyancy, respectively (Eq. 25). $\langle \mathrm{Pr}_T \rangle$ is the typical turbulent Prandtl number (13).

	Jet	Plume
$\Gamma =$	0	1
$\mathrm{Ri} =$	0	$8\alpha_p\beta_g/5$
$r_m =$	$2\alpha_j z$	$\frac{6}{5}\alpha_p z$
$w_m =$	$\frac{M_0^{1/2}}{2\alpha_j} z^{-1}$	$\frac{5}{6\alpha_p}\left(\frac{9}{10}\frac{\alpha_p}{\theta_m\beta_g}F_0\right)^{1/3} z^{-1/3}$
$b_m =$	$\frac{F_0}{2\alpha_j\theta_m} M_0^{-1/2} z^{-1}$	$\frac{5F_0}{6\alpha_p\theta_m}\left(\frac{9}{10}\frac{\alpha_p}{\beta_g\theta_m}F_0\right)^{-1/3} z^{-5/3}$

TABLE II. Asymptotic far-field solutions of jets and plumes including turbulence and pressure effects. In the expressions above, M_0 and F_0 are the mean specific momentum and buoyancy fluxes far away from the source.

resolutions. A detailed validation will thus not be repeated here; agreement with existing data will be pointed out in the text and, where appropriate, included in the figures.

III. RESULTS

A. Integral flow statistics

From an integral perspective, the plume dynamics are fully determined by the evolution of the characteristic radius r_m, velocity w_m and buoyancy b_m. For the limiting cases of a pure jet ($\Gamma = 0$) and of a pure plume ($\Gamma = 1$), the scaling of these parameters with the distance from the source takes the form of a power law, which can be derived from the plume equations[4]. Recently[26], these solutions were extended to account for turbulence and pressure effects via the profile coefficient β_g and for differences in the widths of velocity and buoyancy profiles via the coefficient θ_m (Table II). The profile coefficients β_g and θ_m will be defined rigorously in section III C. The streamwise evolution of r_m is shown in Fig. 1(a), confirming the almost identical linear spreading rate for the three simulations considered. Figs 1(b-d) show that the jet and plume both exhibit the expected power-law scaling. The forced plume transitions from a near-field jet-like scaling to a far-field plume-like scaling.

As visible in Fig. 1(a), the outflow boundary condition appears to affect the statistics in the upper part of the domain. This is caused by subtle modification of the mean flow near the outflow boundary, presumably because of slight pressure gradients[34]. These small disturbances affect the integral quantities Q, M and F via the thresholding technique (which is based on $\overline{w}$, see section II). Throughout what follows, all considerations on the dynamics of the flow will therefore be based on the analysis of the flow statistics for $z/r_0 < 50$.

For the two limiting cases J and P, the plume radius $r_m(z)$ is fitted in the far field ($20 < z/r_m < 50$) to the analytical solutions $r_m = a\alpha(z - z_v)$, where z_v is the virtual origin[29] and $a = 2$ for jets and $a = 6/5$ for plumes (see Table II). We obtain $\alpha_j = 0.067$ and $\alpha_p = 0.105$, values that agree well with the literature and provide evidence of enhanced dilution within a plume compared to a jet.

A flux balance parameter $\Gamma(z)$ that takes into account turbulence, pressure effects and differences in profile widths is defined as[26]

$$\Gamma = \frac{5FQ^2}{8\alpha_p\beta_g\theta_m M^{5/2}}, \tag{15}$$

and its variation with height is shown for the three simulations in Fig. 2(a). For simulation J, Γ is identically

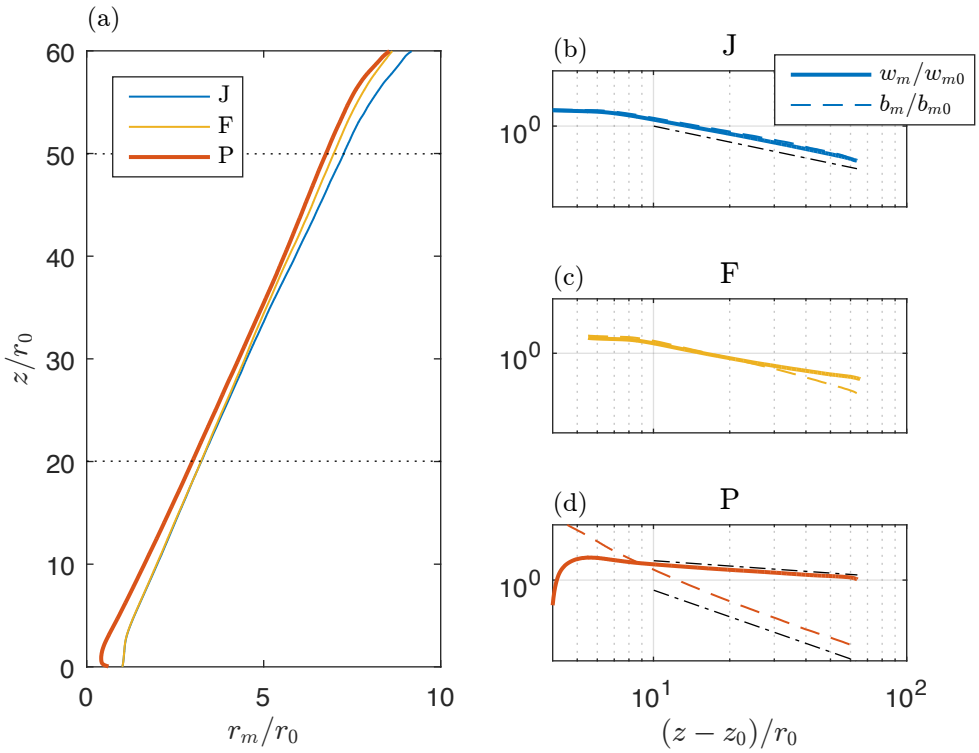

FIG. 1. Variation of the characteristic plume quantities with height z for simulations J, F and P. (a) $r_m(z)$. (b) b_m, w_m for J release. (c) b_m, w_m for F release. (d) b_m, w_m for P release. Dash-dotted lines in Figs (b-d): asymptotic power-law scaling (Table II).

zero for all values of z. For simulation P, $\Gamma \approx 1$ except for a rapid variation in the very near field $z/r_0 < 5$. It is worth noting that for simulation P, the turning points of Γ in the near field are not compatible with classic solutions of the plume equations[15], and have to be attributed to the near-field variations of the profile coefficients (section III C). For forced plume simulation F, Γ evolves approximately linearly towards its equilibrium state $\Gamma = 1$, a condition which is however not attained at the upper limit of the simulated domain.

The variation of the entrainment coefficient α with the vertical coordinate z, as determined from (6), is plotted in Fig. 2(b). Here, Q was filtered to smooth out occasional small step changes in its value caused by the thresholding, which would otherwise result in unphysical spikes in $\mathrm{d}Q/\mathrm{d}\zeta$ and $\alpha(z)$. The values of α_j and α_p (Table I) inferred from r_m are displayed with the dash-dotted lines and are in good agreement with the far-field values for the jet and the plume, respectively. The entrainment in the pure jet shows a high variability in the near field but rapidly attains the constant value α_j, within no more than five source radii. The entrainment coefficient for simulations J and F are almost the same in the near field. However, with increasing distance from the source, the entrainment coefficient in the forced plume simulation F shows a clear increasing trend. For the pure plume, the entrainment coefficient is very large in the near field ($z/r_0 < 5$) and then attains an approximately constant value, which is in close agreement with the far-field estimate $\alpha_p = 0.105$ obtained from r_m. These results are in agreement with previous experimental investigations[9,25], and show a clear tendency of the entrainment coefficient to increase with increasing Γ.

By plotting the computed values of α as a function of Γ, it is possible to test directly the appropriateness of the Priestley and Ball[3] (PB) entrainment model (12) (cf. Fig. 3). Shown in the same plot is the experimental data from Wang and Law[9] (WL02) and the recent measurements from Ezzamel, Salizzoni, and Hunt[25] (ESH15). The latter has been reprocessed in Appendix A to better represent the co-flow in the ambient which significantly influences the entrainment statistics. The new ambient-flow correction shows much better agreement between the volume-flux based estimate of α and that obtained from the entrainment relation, although the data does not display the constant value of α that one would expect from self-similarity in the far field for the jet and plume experiments.

As is evident from Fig. 3, all data sets show a dependence on Γ. The current DNS data set and the WL02

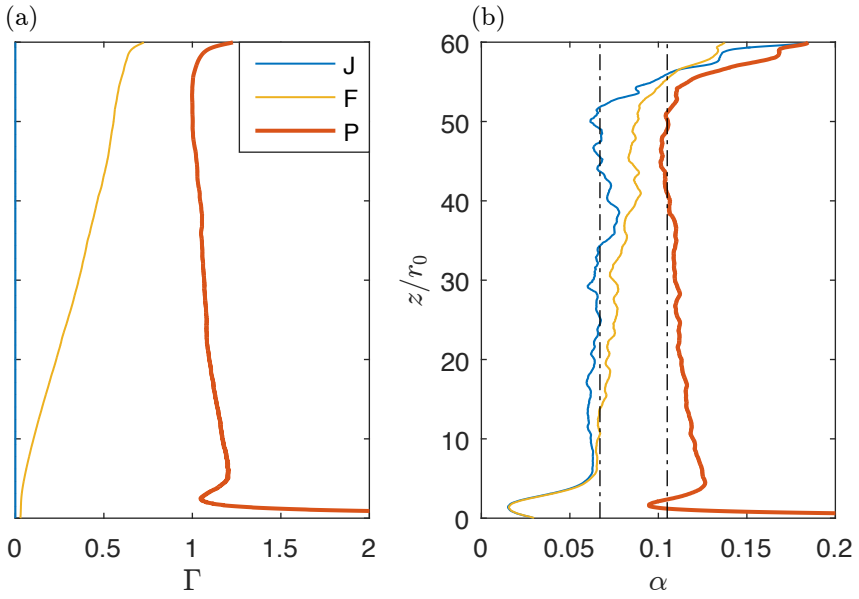

FIG. 2. Vertical evolution for the simulations J, F and P of: (a) the flux balance parameter Γ, and (b) the entrainment coefficient α computed from (6).

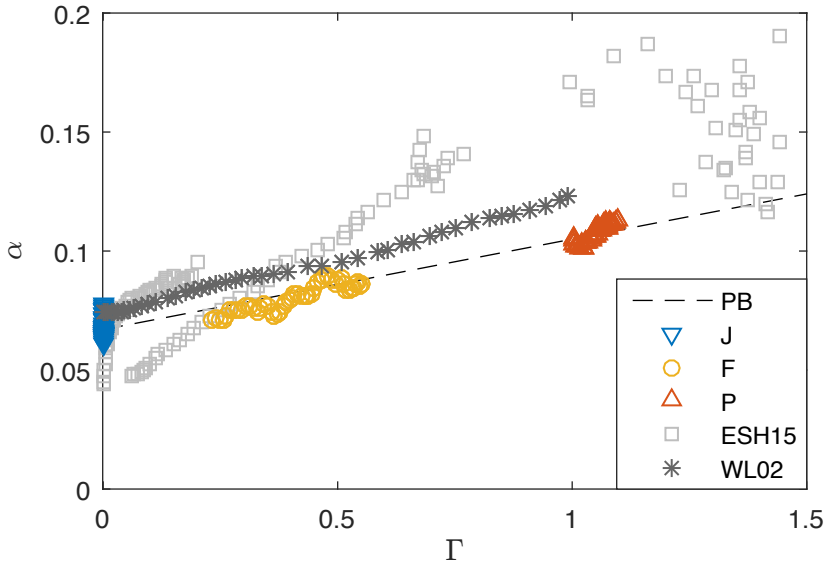

FIG. 3. Entrainment coefficient α as a function of Γ over the interval $20 < z/r_0 < 50$ for simulations J, F and P, confirming the good agreement with the Priestley and Ball [3] (PB) entrainment model. Data of Wang and Law [9] (WL02) and Ezzamel, Salizzoni, and Hunt [25] (ESH15) are also shown.

data convincingly demonstrate the linear dependence on Γ of the Priestley and Ball entrainment model (12) for unstratified environments in the self-similar regime. However, the figure also exposes the variability in what may be regarded as the limiting (or end member) entrainment coefficients; the values one would choose for α_j and α_p in (12) would be slightly different for the WL02 and current data set. The dashed line shows the PB entrainment model using the values of α_j and α_p presented in Table I, and good agreement with the DNS data can be observed. The ESH15 data confirms the appropriateness of the PB model qualitatively, but despite the ambient-flow correction (Appendix A) the data remains noisy. The linear dependence of α on Γ implies that δ_m is practically identical in jets and plumes, as argued in the Introduction. The entrainment coefficient will be decomposed into its various parts in section III D.

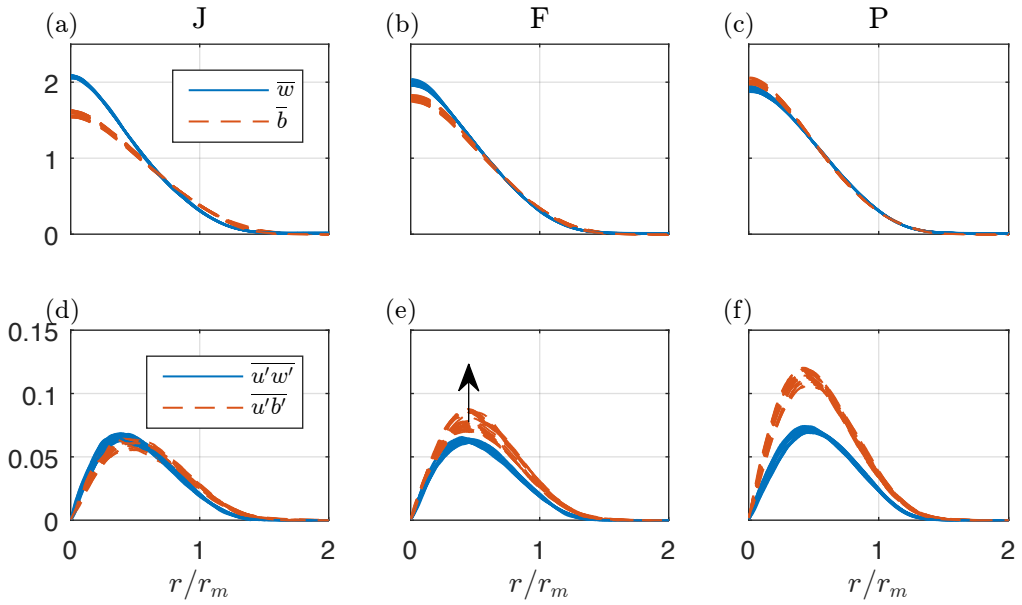

FIG. 4. Self-similarity profiles of $\overline{w}$, $\overline{b}$, $\overline{u'w'}$ and $\overline{u'b'}$ over the interval $20 < z/r_0 < 50$. (a,d): jet simulation. (b,e): forced plume simulation. (c,f): pure plume simulation.

B. Self-similarity

Shown in Fig. 4 are the mean velocity $\overline{w}$, buoyancy $\overline{b}$, radial turbulent momentum flux $\overline{u'w'}$ and turbulent buoyancy flux $\overline{u'b'}$ over the vertical interval $20 < z/r_0 < 50$. As is customary, all variables are presented in dimensionless form, normalised by the local value of r_m, b_m and w_m. In line with our expectations, for all three simulations the mean vertical velocity $\overline{w}$ collapses onto a single profile which closely resembles a Gaussian profile.

The radial profiles of mean buoyancy $\overline{b}$ also exhibit a clear Gaussian-like dependence on the radial coordinate. However, the centreline values and spread differ for the three simulations. Profiles for velocity and buoyancy almost coincide for plumes (Fig. 4(c)), whereas for the forced plume and the jet, the buoyancy profiles have a slightly larger spread (as further quantified by the profile coefficient θ_m associated with mean scalar transport, see section III C). As the integral under the dimensionless curves is unity by construction, a wider profile will reduce the centreline value of $\overline{b}/b_m$, particularly since small changes far from the centreline contribute significantly to the integral due to the conical geometry.

The profile of the turbulent radial momentum flux $\overline{u'w'}$ is practically identical for the jet, forced plume and pure plume (Figs 4(d-f)), which is consistent with the notion of the profile coefficient associated with the production of turbulence kinetic energy δ_m being insensitive to Γ. However, the normalised radial turbulent buoyancy flux shows large variations in amplitude. For the jet simulations, the profiles of $\overline{u'w'}$ and $\overline{u'b'}$ are practically identical. For the plume simulation, $\overline{u'b'}$ is about 60% larger in amplitude than $\overline{u'w'}$. The profile of $\overline{u'b'}$ for the forced plume transitions smoothly from the jet profile to the plume profile as Γ tends to unity, as indicated by the arrow in Fig. 4(e); this is in contrast to Fig. 4(f), where no systematic variation with height is present.

The normalised mean radial velocity $\overline{u}$ is shown in Fig. 5(a). Contrary to the mean vertical velocity $\overline{w}$ profiles, the shape of $\overline{u}$ differs significantly between the jet, forced plume and pure plume. For the jet, $\overline{u}$ increases from a value of zero (imposed by the radial symmetry of the flow), reaches a peak at $r/r_m \approx 0.5$, then decreases, becomes negative with a minimum at $r/r_m \approx 1.4$, after which the velocity $\overline{u}$ decays approximately inversely proportional to the radius due to the fact that the flow varies very slowly with z. For the plume, the maximum in $\overline{u}$ is significantly smaller, implying a reduction in the mean outward radial transport in a plume. The normalised specific radial volume flux $r\overline{u}/(r_m w_m)$, shown in Fig. 5(b) for all three simulations, tends to a constant value outside the plume for $r/r_m > 1.5$. By rearranging Eq. (5), it clear that the constant value is equal to the entrainment coefficient α. The dashed lines in Fig. 5(b) are the values of α in Table I – excellent agreement is shown with the values deduced from r_m.

The turbulent components $\overline{u'u'}$ and $\overline{v'v'}$, shown as a function of r/r_m in Figs 6(a-c), are self-similar and

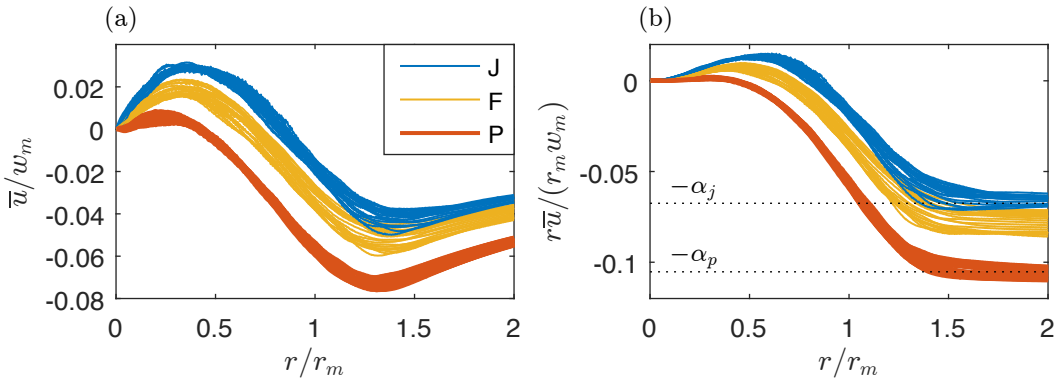

FIG. 5. (a) Self-similar profiles for mean radial velocity $\overline{u}$. (b) Normalised mean radial specific volume flux. The dotted lines indicates the values of α_j and α_p in Table I.

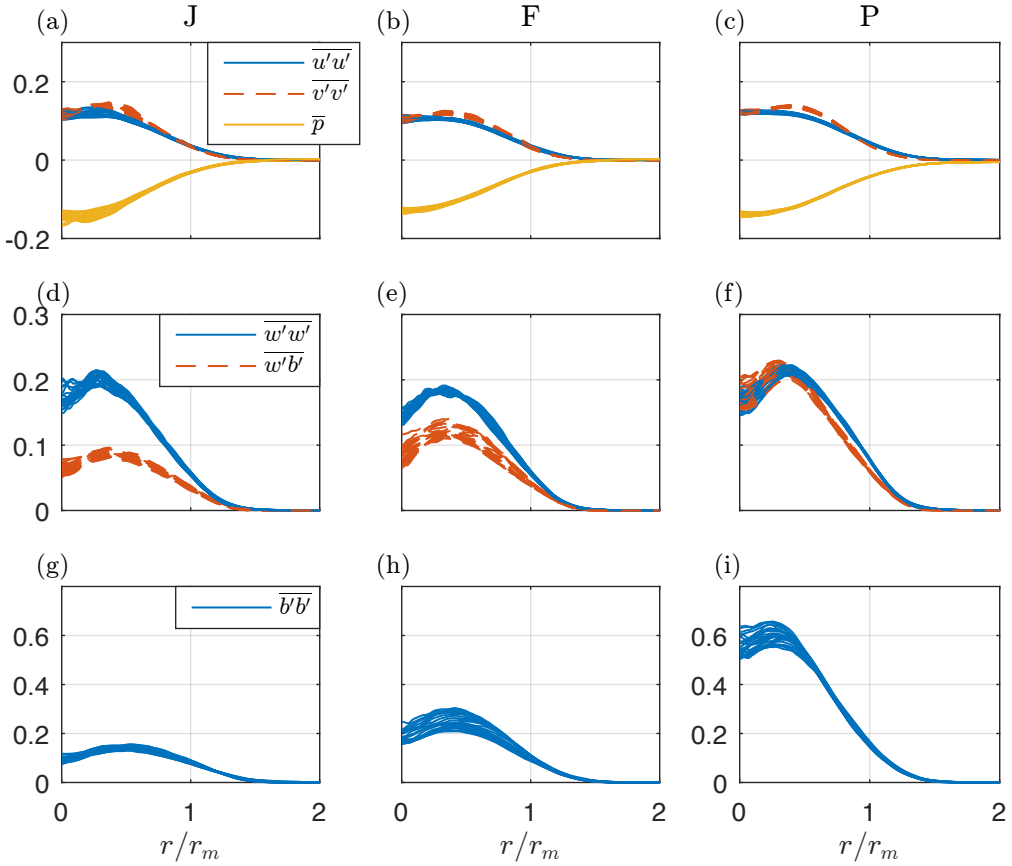

FIG. 6. Self-similarity profiles of second-order quantities and pressure. All quantities are normalised.

practically identical. Furthermore, their dependence on Γ is negligible, providing further confirmation that the turbulence inside plumes and jets is similar, at least in terms of the second-order statistics. The mean pressure $\overline{p}$ is extremely difficult to measure in laboratory experiments, and is usually approximated by[9,25,37] $\overline{p} \approx -(\overline{u'u'} + \overline{v'v'})/2$. The quantity $\overline{p}$ is readily available in DNS and it is clear from Figs 6(a-c) that it correlates well with $-(\overline{u'u'} + \overline{v'v'})/2$, although upon closer inspection (Fig. 7) it becomes evident that $-(\overline{u'u'} + \overline{v'v'})/2$ underestimates $\overline{p}$ by 30% in the core of the flow, whilst it overestimates $\overline{p}$ by about 10% near $r/r_m = 1$. Thus, the DNS data demonstrates that $\overline{p} = -(\overline{u'u'} + \overline{v'v'})/2$ within, say, 20% (see Hussein, Capp, and George[37] for a detailed explanation of the various sources of error). Like the gradient of all quantities in a slender turbulent boundary layer, the gradient of pressure in the radial direction is expected

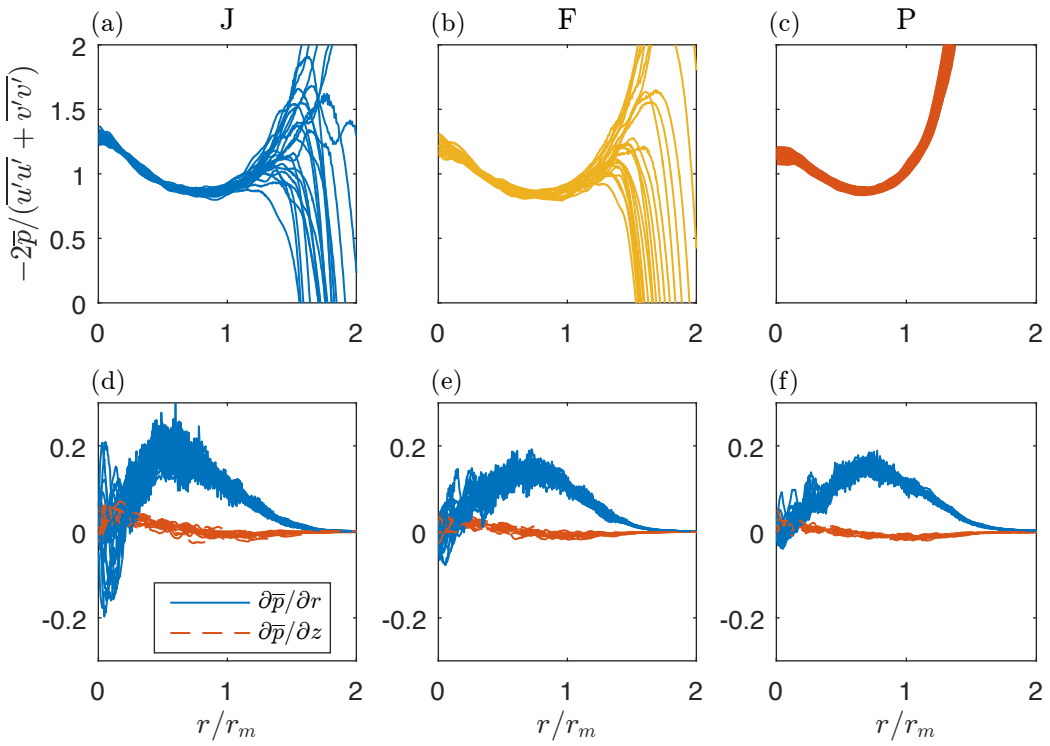

FIG. 7. (a-c) The ratio of mean pressure $\overline{p}$ and $-(\overline{u'u'}+\overline{v'v'})/2$. (d-f) The horizontal and vertical pressure gradients. (a,d) Simulation J. (b,e) Simulation F. (c,f) Simulation P.

to be larger than in the vertical direction by a factor proportional to the spreading rate of the flow. The DNS data confirms that this is the case (Figs 7(d-f)).

Figs 6(d-f) show the streamwise turbulent momentum and buoyancy flux. Whilst the vertical turbulent momentum flux is more or less identical for cases J, F and P, the buoyancy profile differs significantly between the three subplots. Clearly, an increase in the value of Γ increases the vertical turbulent buoyancy flux, as well as the radial buoyancy flux (Figs 4(d-f)). A similar trend is observable in the turbulence buoyancy variance (Figs 6(g-i)). Note that given a sufficient vertical extent of the domain, we expect both $\overline{w'b'}$ and $\overline{b'b'}$ for simulation F to increase to levels observed in simulation P.

To provide further evidence of the similarity of the turbulence statistics in plumes and jets it is instructive to calculate the invariants of the anisotropy tensor[38]

$$b_{ij} = \frac{\overline{u_i' u_j'}}{2e} - \frac{1}{3}\delta_{ij}, \tag{16}$$

where $e = \frac{1}{2}\overline{u_i' u_i'}$ is the turbulence kinetic energy and δ_{ij} is the Kronecker delta. As the turbulence is incompressible, one invariant of $\mathbf{b}$ is zero, and the other two, denoted ξ and η, are defined via $\mathrm{Tr}(\mathbf{b}^2) \equiv 6\xi^2$ and $\mathrm{Tr}(\mathbf{b}^3) \equiv 6\eta^3$, where Tr denotes the tensor trace. The invariants of $\mathbf{b}$ cannot take any value; realisable flows are confined to a region of the $\xi - \eta$ space commonly known as the Lumley triangle[38].

The invariants are calculated as follows. The second-order statistics shown in Figs 4 and 6 are averaged over the range $20 < z/r_m < 50$, after which ξ and η are calculated as a function of r/r_m. Figs 8(b, c) show, respectively, the profiles of invariants η and ξ as a function of r/r_m. It is evident that the profiles for J, F and P are nearly indistinguishable for $r/r_m < 1.5$, providing further evidence that turbulence in jets and plumes is similar. In the $\xi - \eta$ plane (Fig. 8(a)), the data is close to the $\xi = \eta$ line, which is indicative of axisymmetric turbulence with one large eigenvalue, i.e. rod-like turbulence. Interestingly, at the edge of the jet/plume, ξ changes very rapidly from positive to negative. For plumes, the crossover appears to happen closer to the centreline than for the jet. Thus, near the plume edge, the average picture of the turbulence resembles axisymmetric turbulence with one small eigenvalue, i.e. disk-like turbulence. These observations are in agreement with the laboratory experiments of Hussein, Capp, and George[37], which were presented in terms of the (ξ, η) invariants in Kuznik, Rusaouen, and Brau[39].

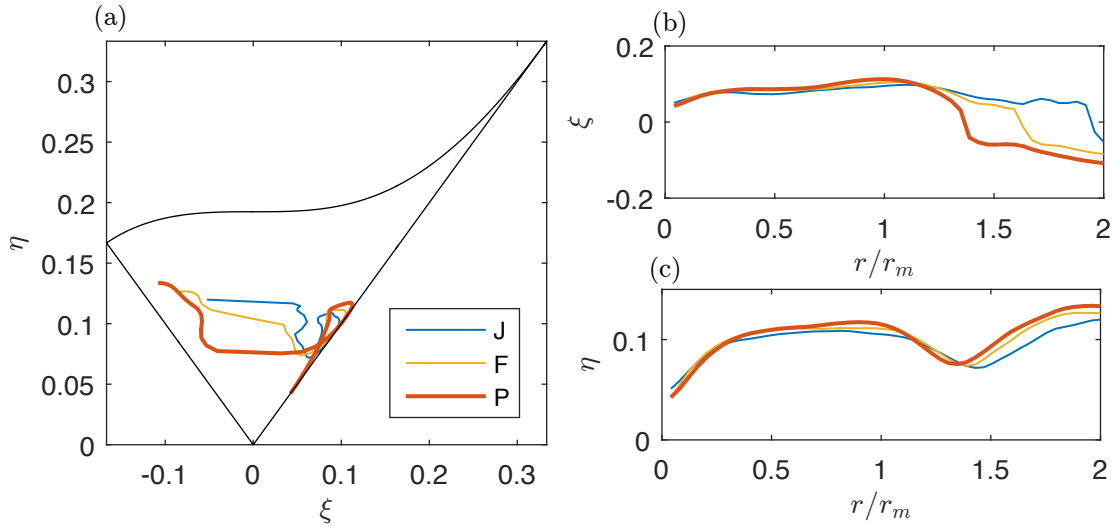

FIG. 8. Invariants of the anisotropy tensor (16) for the jet, forced plume and plume. (a) Plot in $\xi-\eta$ space, together with the Lumley triangle. (b) Dependence of ξ on r/r_m. (c) Dependence of η on r/r_m.

Consideration of the vertical gradient $\partial\overline{w}/\partial z$ provides a possible explanation for why the point at which turbulence changes from being dominated by one component (the core region) to two components (the edge of the flow) differs in jets compared with plumes. Noting that $w_m \sim z^{-1}$ in jets, whereas $w_m \sim z^{-1/3}$ in plumes, the point at which $\partial\overline{w}/\partial z = 0$ occurs at larger values of r/r_m in jets than it does in plumes. Likening the flow with a diverging (core region, $\partial\overline{w}/\partial z < 0$) or converging (edge region, $\partial\overline{w}/\partial z > 0$) nozzle, one would therefore expect the point of transition between one-component and two-component regimes, respectively, to be affected by differences in the point at which $\partial\overline{w}/\partial z$ changes sign.

C. Profile coefficients

Profile coefficients encapsulate integrated information about mean and turbulent fluxes of momentum, buoyancy, mean kinetic and turbulence production. In classic integral descriptions of the plume equations[4], the profile coefficients are generally assumed to be either unity or zero. However, preserving information about profile shapes is crucial in the description of unsteady jets and plumes[35,36,40], and is also the key to decomposing entrainment into its various processes. The profile coefficients for momentum (β), buoyancy (θ), energy (γ) and turbulence production (δ) are given by, respectively:

$$
\begin{aligned}
&\beta_m \equiv \frac{M}{w_m^2 r_m^2} \equiv 1, && \beta_f, \equiv \frac{2}{w_m^2 r_m^2}\int_0^\infty \overline{w'^2} r\mathrm{d}r, && \beta_p \equiv \frac{2}{w_m^2 r_m^2}\int_0^\infty \overline{p} r\mathrm{d}r,\\
&\gamma_m \equiv \frac{2}{w_m^3 r_m^2}\int_0^\infty \overline{w}^3 r\mathrm{d}r, && \gamma_f \equiv \frac{4}{w_m^3 r_m^2}\int_0^\infty \overline{w}\,\overline{w'^2} r\mathrm{d}r, && \gamma_p \equiv \frac{4}{w_m^3 r_m^2}\int_0^\infty \overline{wp} r\mathrm{d}r,\\
&\delta_m \equiv \frac{4}{w_m^3 r_m}\int_0^\infty \overline{w'u'}\frac{\partial\overline{w}}{\partial r} r\mathrm{d}r, && \delta_f \equiv \frac{4}{w_m^3 r_m}\int_0^\infty \overline{w'^2}\frac{\partial\overline{w}}{\partial z} r\mathrm{d}r, && \delta_p \equiv \frac{4}{w_m^3 r_m}\int_0^\infty \overline{p}\frac{\partial\overline{w}}{\partial z} r\mathrm{d}r,\\
&\theta_m \equiv \frac{F}{w_m b_m r_m^2}, && \theta_f \equiv \frac{2}{w_m b_m r_m^2}\int_0^\infty \overline{w'b'} r\mathrm{d}r.
\end{aligned}
\tag{17}
$$

The total momentum flux is given by $\beta_g M$, where $\beta_g = \beta_m+\beta_f+\beta_p$. Similarly, θ_g is associated with the total buoyancy flux, γ_g with the total energy flux and δ_g with the total turbulence production (including pressure redistribution). Profile coefficients β and θ show up naturally upon radial integration of the Reynolds-averaged volume, vertical momentum and buoyancy equations of a high Reynolds number flow in a neutral environment[26]

$$
\frac{1}{Q}\frac{\mathrm{d}Q}{\mathrm{d}\zeta} = 2\alpha, \qquad \frac{1}{M}\frac{\mathrm{d}}{\mathrm{d}\zeta}\left(\beta_g M\right) = \mathrm{Ri}, \qquad \frac{1}{F}\frac{\mathrm{d}}{\mathrm{d}\zeta}\left(\frac{\theta_g}{\theta_m}F\right) = 0. \tag{18a-c}
$$

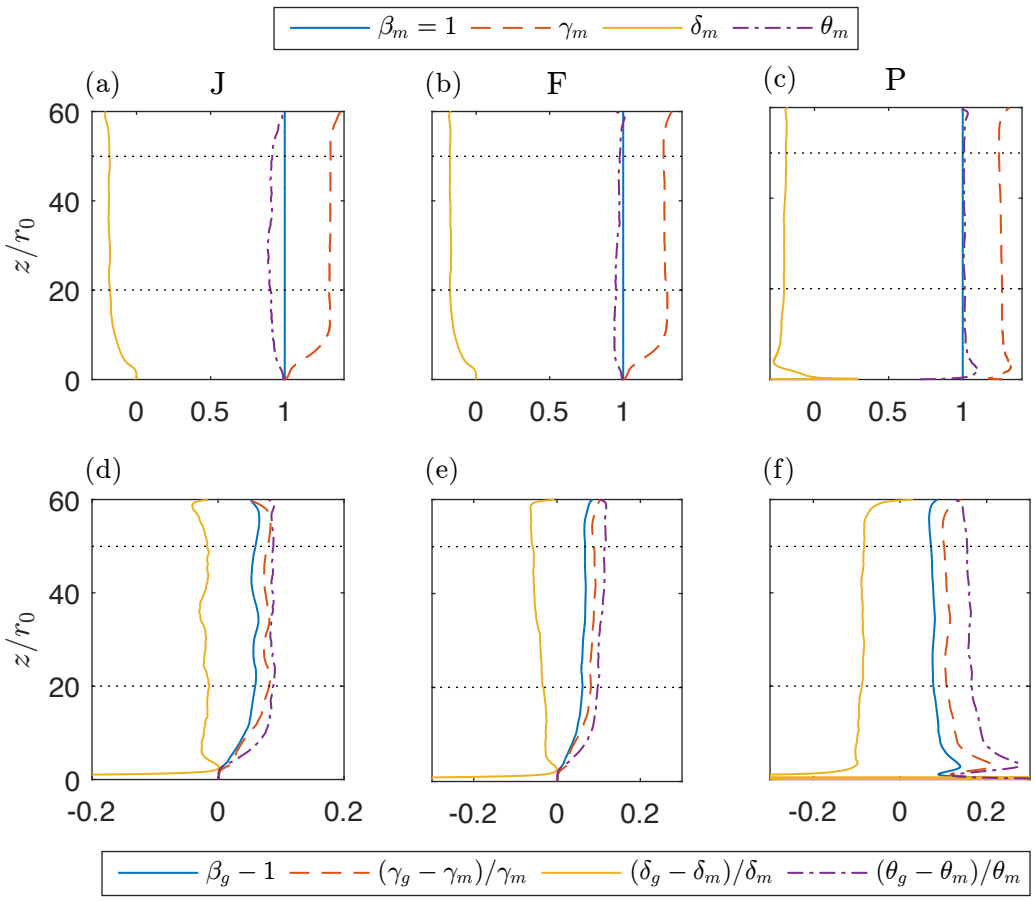

FIG. 9. (a-c) Mean profile coefficients. (d-f) The relative contribution of turbulence and pressure to the dimensionless coefficients. (a,d) Simulation J. (b,e) Simulation F. (c,f) Simulation P. The dashed lines indicate the averaging interval $20 < z/r_0 < 50$ used for the profile coefficients displayed in Table III.

These equations reduce to the classic plume equations[4] on setting $\beta_g = 1$ and $\theta_g = \theta_m = 1$. Furthermore, we note that $\mathrm{Ri} = 0$ by definition for the jet, implying that the evolution of F and M are uncoupled (and that F in that case corresponds to a passive scalar flux). Similarly, γ and δ emerge naturally from integration of the mean kinetic energy equation:

$$\frac{Q}{M^2}\frac{\mathrm{d}}{\mathrm{d}\zeta}\left(\gamma_g \frac{M^2}{Q}\right) = \delta_g + 2\theta_m \mathrm{Ri}. \tag{19}$$

Fig. 9 shows the profile coefficients as a function of z. The coefficients associated with the mean flow, β_m, γ_m, δ_m and θ_m, are shown in Figs 9(a-c). There are large variations in the profile coefficients in the near field, which are due to changes in the velocity and buoyancy profiles as the jet/plume develops; indeed, the largest changes occur over a small region $z/r_0 < 5$, for the plume even closer to the source ($z/r_0 < 3$). However, for larger z/r_0 the coefficients become constant, which is consistent with self-similarity.

The average values of the profile coefficients over the interval $20 < z/r_0 < 50$ are presented in Table III. The dimensionless buoyancy flux θ_m is less than unity for the jet, implying that the spread of the buoyancy field exceeds the spread of the velocity field. This can be shown by assuming a Gaussian form for the velocity and buoyancy profiles

$$\overline{w} = 2w_m \exp\left(-2\frac{r^2}{r_m^2}\right), \qquad \overline{b} = 2\frac{b_m}{\varphi^2}\exp\left(-2\frac{r^2}{\varphi^2 r_m^2}\right), \tag{20}$$

where φr_m is the characteristic width of the buoyancy profile and φ is the ratio of the buoyancy to velocity radii. These profiles are consistent with the definitions $\beta_m = 1$ and $B = b_m r_m^2$, and evaluation of the profile coefficient for the mean energy flux results in $\gamma_m = 4/3$. The buoyancy flux is given by $F = 2\int_0^\infty \overline{w}\overline{b} r \mathrm{d}r =$

	J	F	P
β_f	0.151	0.149	0.183
β_u	0.095	0.088	0.106
β_v	0.102	0.095	0.110
β_p	-0.093	-0.084	-0.107
β_g	1.058	1.065	1.076
γ_m	1.306	1.282	1.256
γ_f	0.276	0.267	0.319
γ_p	-0.175	-0.156	-0.183
γ_g	1.406	1.393	1.391
δ_m	-0.184	-0.175	-0.201
δ_f	0.006	0.016	0.038
δ_p	-0.002	-0.008	-0.021
δ_g	-0.180	-0.167	-0.184
θ_m	0.901	0.964	1.011
θ_f	0.078	0.103	0.162
θ_g	0.979	1.067	1.172

TABLE III. Average profile coefficients over the interval $20 < z/r_0 < 50$.

$\frac{2}{\varphi^2+1} w_m b_m r_m^2$. By substituting this expression into the definition of profile coefficient θ_m (17), it directly follows that

$$\theta_m = \frac{2}{\varphi^2 + 1}. \tag{21}$$

For the plume, $\theta_m \approx 1$, implying that $\varphi \approx 1$ also. The value of θ_m for the forced plume tends to become closer to unity with increasing z. The dimensionless turbulence production δ_m shows differences of the order of 10% between the jet and the plume (see also Table III), which is too small to explain the observed differences in α (see section III D).

Figs 9(d-f) show the relative contribution of turbulence and pressure terms to the total, which are neglected in classic plume theory. Gradual changes can be observed in the far-field which are caused by the fact that the second-order statistics require a greater vertical distance to become fully self-similar than the first-order statistics. Indeed, Wang and Law [9] observed that full self-similarity of the turbulence statistics did not occur before $z/r_0 \approx 100$, which is nearly twice the vertical extent of our domain. However, it is clear that in general, the influence of turbulence and pressure is less than 10% of the mean value, which partially explains why plume theory provides such robust predictions for plume behaviour. The largest deviations between mean and total are found in θ, the dimensionless buoyancy flux, which for plumes is as high as 20%, consistent with literature[32,41]. Here, we would like to point out that θ_f is a source of systematic error in laboratory experiments where the (total) buoyancy flux is usually determined *a priori* (nozzle volume flux $\times$ buoyancy). However, plume theory only considers means, and the mean buoyancy flux is about 20% less than the total buoyancy flux. Indeed, we find good agreement of the DNS data with the classic solutions of plume theory only by explicitly calculating the mean buoyancy flux.

D. Decomposing the entrainment coefficient

As shown in van Reeuwijk and Craske [26], taking (6) as a definition of α, and using (19) and (18b), α can be decomposed as:

$$\alpha = \underbrace{-\frac{\delta_g}{2\gamma_g}}_{\alpha_{prod}} + \underbrace{\left(\frac{1}{\beta_g} - \frac{\theta_m}{\gamma_g}\right) \mathrm{Ri}}_{\alpha_{\mathrm{Ri}}} + \underbrace{\frac{\mathrm{d}}{\mathrm{d}\zeta}\left(\log \frac{\gamma_g^{1/2}}{\beta_g}\right)}_{\alpha_{shape}}. \tag{22}$$

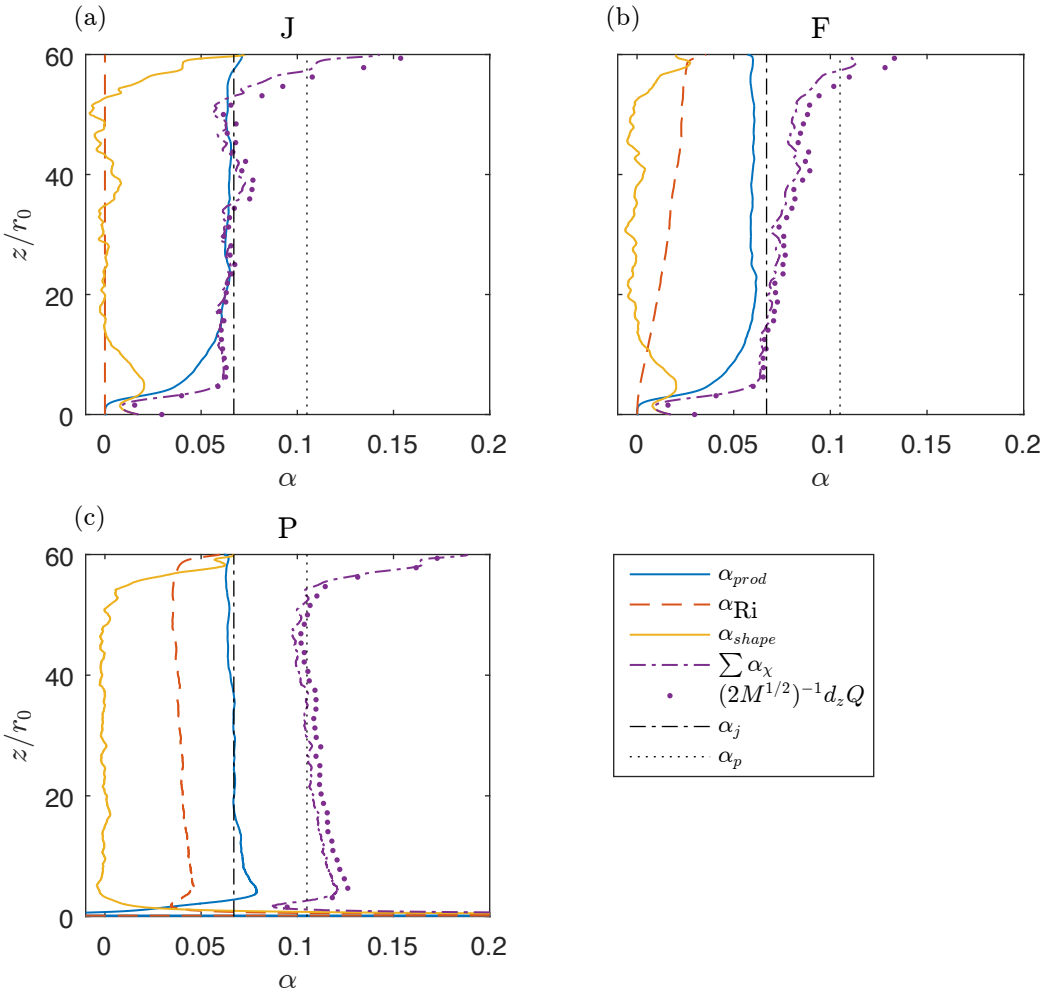

FIG. 10. Evolution of the contribution to entrainment due to turbulent kinetic energy production α_{prod}, buoyancy α_{Ri} and departure from self-similarity α_{shape}, as a function of z. Note that in the legend, $\sum \alpha_\chi = \alpha_{prod} + \alpha_{\mathrm{Ri}} + \alpha_{shape}$.

The entrainment relation (22) quantifies the contribution to α of turbulence production α_{prod}, mean buoyancy α_{Ri} and changes in profile shape α_{shape}. The vertical evolution of the individual contributions to α, as well as the direct estimate of α using (6) and the estimate of α using r_m (Table I) are plotted in Fig. 10. The three estimates of α are in good agreement with each other, demonstrating the consistency of the data with the underlying integral equations. The analysis of data from the plume literature carried out in van Reeuwijk and Craske [26] (VRC15) highlighted that δ_m, and thus α_{prod}, was approximately identical in jets and plumes. This is convincingly confirmed in Fig. 10(c), as α_{prod} matches closely with the value of α_j inferred from the jet data. For the forced plume, α_{prod} is slightly lower than α_j but remains in good agreement. The mean-flow contribution of buoyancy to α is constant for simulation P, and has a magnitude of $2\alpha_j/3$. For simulation F, α_{Ri} can be observed to increase with height.

The term α_{shape} will only be non-zero when the profiles of first- and second-order statistics change in shape, i.e. when the profiles are not self-similar. Non-self-similar behaviour is dominant in the near field, where the flow transitions to turbulence and the mean profiles attain their Gaussian shapes. The near-field region, within which α_{shape} is different from zero, extends up to about 15 source diameters for the jet and the forced jet, and only for about 5 source diameters for the plume.

Next, we explore the concept of similarity drift, which pertains to a possible variation in z of the ratio of buoyancy to velocity profile width $\varphi(z)$. The concept of similarity drift can be traced back to Kaminski, Tait, and Carazzo [17] (KTC05), who derived an entrainment relation that contains a term of the form

$$\alpha_e = \ldots + \frac{1}{2} R \frac{\mathrm{d}}{\mathrm{d}z} \log A, \tag{23}$$

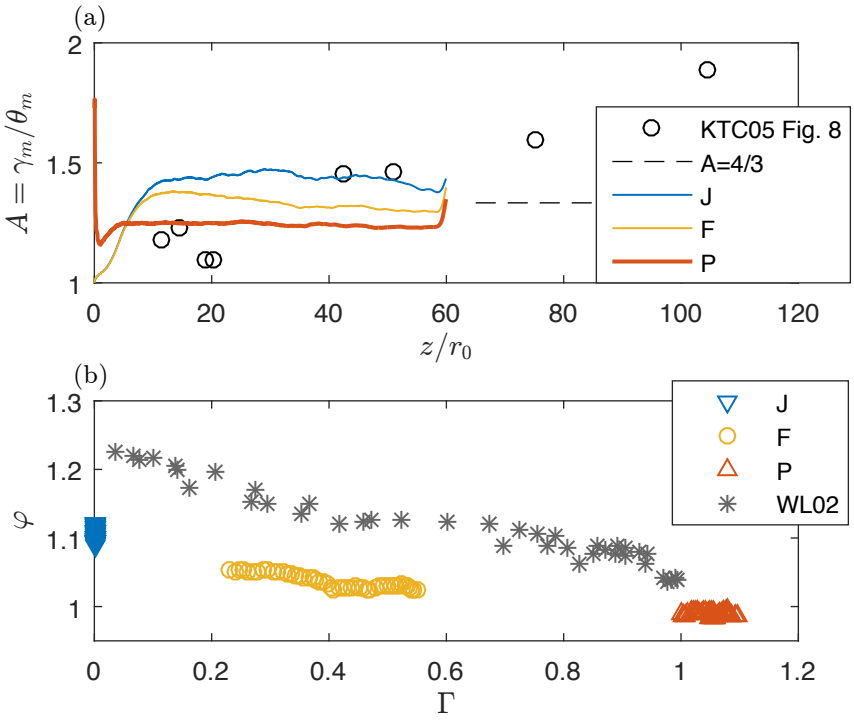

FIG. 11. Exploration of similarity drift. (a) $A = \gamma_m/\theta_m$ as a function of z/r_0. (b) φ as a function of Γ.

where R is a typical radius, $A = \gamma_m/\theta_m = \gamma_m(1+\varphi^2)/2$ and α_e is an entrainment coefficient that is related[26], but not identical to α (α_e uses non-standard characteristic scales in KTC05, implying that the α_{shape} in the entrainment relation in terms of α (22) is independent of θ). Hence, (23) indicates that changes in A, e.g. because of a drift $\varphi = \varphi(z)$ will have a non-zero contribution to α_e. In KTC05, the value A was calculated for published data which, despite significant scatter, showed an increasing trend of A with the distance from the source.

Fig. 11(a) shows the experimental data collected from Fig. 8 in KTC05 together with the new DNS data set discussed in this article. Unlike the experimental data, the DNS data does not imply that A varies as a function of z. Indeed, it is unclear what physical mechanism could be responsible for producing similarity drift. Full self-similarity of the process results from an asymptotically small dependence on the source conditions and ambient conditions that scale in the same way as the local behaviour of the plume. We therefore suggest that the similarity drift observed in experiments is caused by the absence of an ideal undisturbed, unbounded ambient environment (including confinement effects) or a persistent dependence of the process on source conditions.

The DNS and WL02 data suggest a relation between φ and Γ, see Fig. 11(b). As for Fig. 3, the DNS and WL02 data show that φ is a decreasing function of Γ, tending to $\varphi \approx 1$ at $\Gamma = 1$. The Γ-dependence is more pronounced for the WL02 data than the DNS data, the reason for which is unclear.

E. Turbulent transport

The turbulent radial transport of streamwise momentum $\overline{u'w'}$ and buoyancy $\overline{u'b'}$ are crucial in determining the profile shape and entrainment behaviour of jets and plumes. These quantities can be related to the mean fields using the gradient diffusion hypothesis, i.e.

$$\overline{u'w'} = -\nu_T \frac{\partial \overline{w}}{\partial r}, \qquad \overline{u'b'} = -D_T \frac{\partial \overline{b}}{\partial r}. \tag{24}$$

These quantities were computed using $\nu_T/(w_m r_m) = -f_{uw}/f_w'$ and $D_T/(w_m r_m) = -f_{ub}/f_b'$, where the similarity functions f_χ are the averages of those presented in Fig. 4 and the prime denotes differentiation with respect to η. The results are shown in Figs 12(a,b) for the jet and plume, respectively. The radial

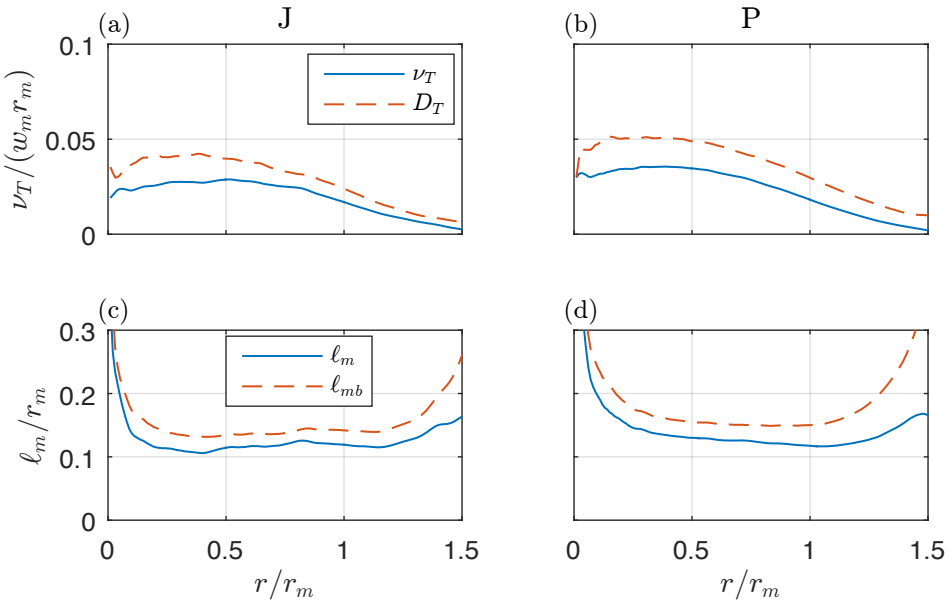

FIG. 12. Radial profiles of ν_T and D_T: (a) for the jet and (b) and for the pure plume. Radial mixing length radial profiles: (c) for the jet and (d) for the pure plume.

distributions of ν_T and D_T have a similar shape, with D_T systematically higher than ν_T for both the jet and the plume. The values for ν_T and D_T are slightly higher for the plume than for the jet.

The profiles for ν_T and D_T show substantial variations over the interval $0 < r/r_m < 1$. A Prandtl mixing length model[42] with mixing lengths for momentum and buoyancy of the form $\ell_m = a_w r_m$ and $\ell_{mb} = a_b r_m$, resulting in

$$\frac{\nu_T}{w_m r_m} = a_w^2 |f_w'|, \qquad \frac{D_T}{w_m r_m} = a_b^2 |f_w'|, \tag{25}$$

provides values of $\ell_m/r_m \equiv a_w$ and $\ell_{mb}/r_m \equiv a_b$, that are roughly constant in the core region (Figs 12(c,d)). Very close to the centreline, the mixing length becomes very large because $|f_w'|$ and $|f_b'|$ tend to zero. For $r/r_m > 1$, the mixing length concept does not work well, which we attribute to intermittency effects associated with the plume edge. The typical values for a_w and a_b over the region $0.3 < r/r_m < 1.0$ are presented in Table I. Estimates of the mixing length show a remarkable agreement with the experimental results recently presented by Ezzamel, Salizzoni, and Hunt[25], who estimated the Eulerian integral length scale of the two-point velocity statistics (their figure 15). In particular, note that the measurements revealed almost constant values of the Eulerian integral length in the core of the plume, for both jets and plumes.

The turbulent Prandtl number Pr_T is a quantity of great relevance because of its extensive use in turbulence modelling. By substituting (24) into (13), one obtains

$$\mathrm{Pr}_T = \frac{\nu_T}{D_T} = \frac{f_{uw}}{f_{ub}} \frac{f_b'}{f_w'}. \tag{26}$$

Thus, Pr_T can be thought of as the product of two ratios: 1) the ratio of the radial turbulent fluxes f_{uw}/f_{ub} and 2) the ratio of gradients of the mean buoyancy and velocity f_b'/f_w'. The turbulent Prandtl number, plotted in Fig. 13, is almost constant over the entire cross section with values in the range 0.6 - 0.8. The average value $\langle \mathrm{Pr}_T \rangle$ over the interval $0.3 < r/r_m < 1.0$ is 0.72 for the jet simulation and 0.67 for the plume simulation (see also Table I). Thus, the estimates of $\langle \mathrm{Pr}_T \rangle$ are remarkably close, despite the effect of buoyancy on the plume's behaviour. Shown in Fig. 13(b) is the ratio f_b'/f_w'. For the plume, the ratio is approximately unity, but for the jet it is significantly lower due to the fact that $\theta_m < 1$ and thus $\varphi > 1$. The ratio f_{uw}/f_{ub}, shown in Fig. 13(c), is approximately constant for the plume with a value of about 0.6. For the jet, f_{uw}/f_{ub} decreases slowly with an average value of about 1.

Thus, although Pr_T is very similar for plumes and jets, the reason is different: for jets it is caused primarily by f_b'/f_w' which is associated with the ratio of widths φ, and for the plume primarily by the turbulent flux

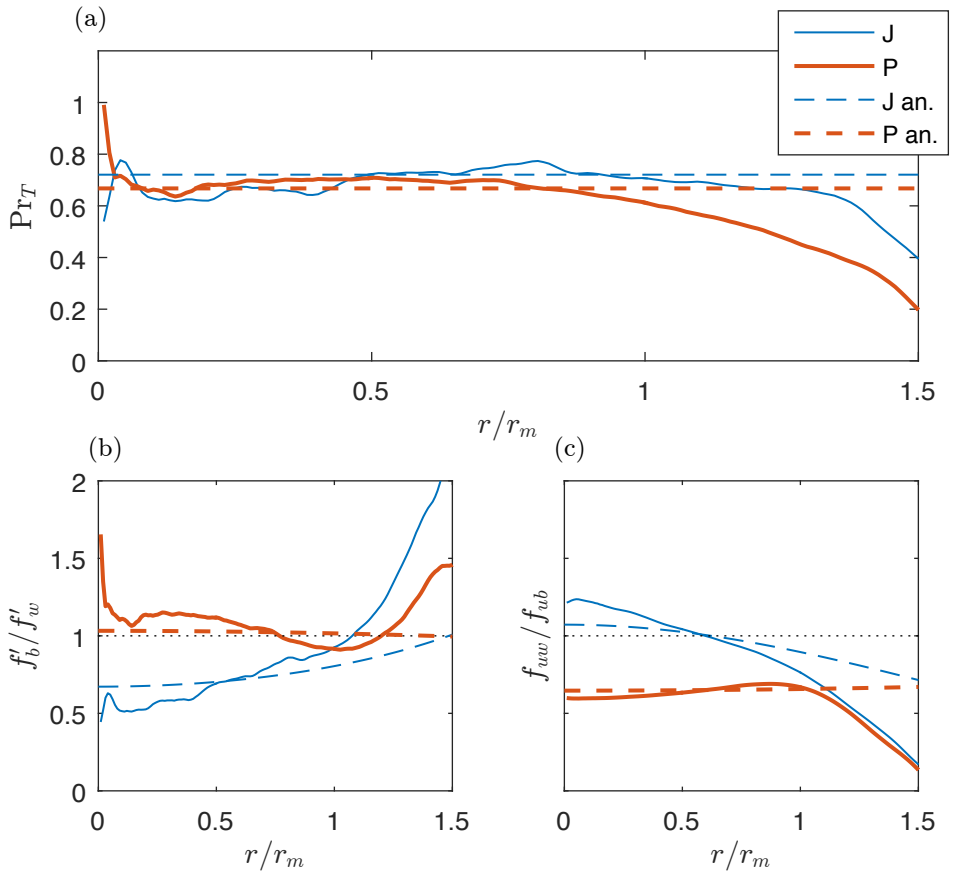

FIG. 13. Radial profiles (a) of the turbulent Prandtl number Pr_T, (b) of the ratio of the similarity functions f_b'/f_w' and (c) f_{uw}/f_{ub} (see text). Solid lines: DNS data. Dashed lines: analytical predictions (27).

ratio f_{uw}/f_{ub}, see also Fig. 4. This can be made explicit by evaluating the ratios (by substituting the Gaussian profiles for $f_w = \overline{w}/w_m$ and $f_b = \overline{b}/b_m$ (20)) into (24), (25), resulting in

$$\frac{f_b'}{f_w'} = \frac{1}{\varphi^4}\exp\left(-\frac{\varphi^2-1}{\varphi^2}\frac{r^2}{r_m^2}\right), \qquad \frac{f_{uw}}{f_{ub}} = \varphi^4\frac{a_w^2}{a_b^2}\exp\left(\frac{\varphi^2-1}{\varphi^2}\frac{r^2}{r_m^2}\right), \tag{27}$$

noting that $(\varphi^2-1)/\varphi^2 = (2-2\theta_m)/(2-\theta_m)$. The product of these two terms evaluates to $\langle \mathrm{Pr}_T\rangle = a_w^2/a_b^2$, consistent with (25). Eq. 27 shows that the amplitude of the ratio f_b'/f_w' is solely determined by the value of φ. The amplitude of the ratio f_{uw}/f_{ub} is determined both by φ and the ratio of mixing lengths a_w/a_b. The theoretical predictions of (27), using parameter values for a_w, a_b from Table I and θ_m from Table III are plotted in Fig. 13 with dashed lines. The results agree quite well in the interval $0 < r/r_m < 1$, both in terms of the amplitude and in the trend. Near the plume edge, it is clear that the mixing lengths and Gaussians do not describe the behaviour.

Previous authors[25] have suggested that a spatially averaged (over the radial plume section) turbulent Prandtl number $\langle \mathrm{Pr}_T\rangle$ can be inferred from the ratio of the plume radii r_m and r_b, estimated through a Gaussian fit of the radial profiles of mean vertical velocity and buoyancy, respectively. For jets this approach is valid because, to leading order, the scalar field and the vertical velocity field essentially obey the same similarity equations, which state that radial mixing must balance the divergence in the vertical flux. As noted previously[43], the ratio of r_m and r_b can be obtained via the substitution of Gaussian profiles into the similarity equations. Evaluation of the resulting balance on the centreline of the flow allows one to relate D_T to r_b and ν_T to r_m. Equivalently, one can view the problem in a moving frame of reference, in which $z^2 \propto t$, and apply the classic relation for diffusion, which predicts that $r_b \propto \sqrt{tD_T}$ and $r_m \propto \sqrt{t\nu_T}$. Both approaches result in $\langle \mathrm{Pr}_T\rangle = \varphi^{-2}$. For jets, we observe that $\varphi \approx 1.1$ and therefore would expect $\langle \mathrm{Pr}_T\rangle \approx 0.8$, which is reasonably consistent with Fig. 13(a). In the case of plumes, however, the analysis described above is not

appropriate, unless one accounts for the additional term arising from buoyancy in the governing momentum equation. Indeed, our results indicate values of $\langle \mathrm{Pr}_T \rangle$ which are systematically lower than unity in plumes (see e.g. Fig. 13(a)), in spite of the fact that $\varphi \approx 1$.

IV. CONCLUSIONS

The dynamics and transport properties of a turbulent pure jet, a pure plume and a forced plume were examined using high-fidelity direct numerical simulations. The motivation for this work, the numerical analogue of the experimental study by Ezzamel, Salizzoni, and Hunt [25], was specifically to shed light on the physical processes linking turbulent transport and entrainment.

The detailed spatial resolution of the DNS allowed the effectiveness of turbulent transport to be quantified, e.g. via turbulent diffusion coefficients and the dilution of fluid in the plume/jet with the ambient. For the forced plume, within which the flow dynamically adjusts towards a pure-plume behaviour asymptotically with height, of particular relevance was the vertical variation of the entrainment coefficient α, numerous models having been proposed to capture this variation. Our results support the Priestley and Ball [3] entrainment model (12) and show that, beyond a near-source region (specifically for $z/r_0 \gtrsim 20$), the entrainment coefficient is a function only of the local Richardson number.

By decomposing α (see (22)) into contributions due to turbulence production, to buoyancy and to shape effects, we show that the production of turbulence due to shear (as represented by the dimensionless quantity δ_m) is practically identical for jets and for plumes, which is indeed the assumption underlying (12). Moreover, since the *turbulent* component of entrainment has been shown to be unaltered by buoyancy[26], this confirms that α is larger for plumes than for jets due to entrainment associated with *mean* flow processes.

The fact that the production of turbulence due to shear takes approximately the same value for jets and plumes suggests that their turbulence structure is quite similar, despite the absence of buoyancy in a jet. The second-order statistics $\overline{u'u'}$, $\overline{v'v'}$ and $\overline{w'w'}$ indeed suggest the turbulence levels are very similar. The invariance of the turbulence anisotropy tensor confirms that turbulence in the core region of a jet/plume is practically indistinguishable. There is, however, evidence of clear distinctions between the structure of a jet and a plume. For example, whilst there is a transition from rod-like to disk-like turbulence moving radially outward from the centreline, this transition occurs closer to the centreline in a plume; these distinctions are believed to be linked with vertical velocity gradients $\partial\overline{w}/\partial z$. Further differences between jets and plumes exist in the second-order scalar statistics, such as $\overline{w'b'}$ and $\overline{b'b'}$. Analysis of the budgets for these quantities would indicate how such differences can exist between flows whose dynamics are similar, and would therefore make a valuable contribution to an overall understanding of turbulence in free-shear flows.

In agreement with existing measurements, the turbulent Prandtl number is found to be almost identical for jets and plumes, taking a value of $\langle \mathrm{Pr}_T \rangle = 0.7$. However, by writing this quantity as the ratio of turbulent fluxes and radial gradients of mean quantities, it becomes evident that for jets, the value of $\langle \mathrm{Pr}_T \rangle$ can be attributed to differences in the ratio of velocity to buoyancy profile widths φ, whereas for plumes, the value of $\langle \mathrm{Pr}_T \rangle$ is associated with the ratio of the turbulent radial transport of buoyancy and streamwise momentum.

The DNS data does not support the notion of similarity drift, and we conjecture that the observed variations in profile widths between experiments are possibly a result of confinement or other deviations from ideal boundary conditions.

ACKNOWLEDGMENTS

We acknowledge the UK Turbulence Consortium (grant number EP/L000261/1) and an EPSRC ARCHER Leadership Grant for providing the computational resources required to carry out the computations. In addition, JC gratefully acknowledges funding from the Engineering and Physical Sciences Research Council (EPSRC) Doctoral Prize under grant number EP/M507878/1. PS gratefully acknowledges the support of Cambridge University's Engineering Department and Peterhouse College in June 2015. Supporting data for this article is available on request: please contact either m.vanreeuwijk@imperial.ac.uk or civilsfluids@imperial.ac.uk.

Appendix A: Ambient-flow correction of the ESH15 data.

The purpose of this appendix is two-fold: 1) to correct the data of Ezzamel, Salizzoni, and Hunt [25] (ESH15) for vertical variation in the ambient flow; and 2) to present the experimental data in terms of the notation used in this paper.

A significant part of the work in ESH15 was associated with the analysis of $\alpha(z)$. The z-dependence of α was determined in two ways: 1) via volume conservation (6); and 2) via the entrainment relation (22) considering mean contributions and self-similarity only, assuming Gaussian profiles ($\gamma_m = 4/3$):

$$\alpha = -\frac{3}{8}\delta_m + \left(1 - \frac{3}{4}\theta_m\right) \mathrm{Ri}. \tag{A1}$$

In ESH15, this relation was presented in terms of the relative plume width $\varphi = \sqrt{2/\theta_m - 1}$, the effective eddy viscosity $\langle\widehat{\nu_T}\rangle = -\delta_m/(8\sqrt{2})$ and the flux balance parameter $\Gamma = 5\mathrm{Ri}/(8\alpha_p)$ (note that $\beta_g = 1$ as only means are considered), i.e. as

$$\alpha_G = 3\langle\widehat{\nu_T}\rangle + (2\varphi^2 - 1)\frac{2\alpha_{pG}\theta_m}{5}\Gamma. \tag{A2}$$

Here, $\alpha_G = \alpha/\sqrt{2}$ is the Gaussian entrainment coefficient and $\alpha_{pG} = \alpha_p/\sqrt{2}$ the Gaussian entrainment coefficient for a pure plume. The prefactor for $\langle\widehat{\nu_T}\rangle$ is a factor two larger than reported in ESH15. Furthermore, the factor θ_m in the buoyancy contribution was not present in ESH15; this is caused by the inclusion of β_g and θ_m in the flux balance parameter Γ (15). Indeed, denoting the classic flux balance parameter[5] by $\Gamma^* = 5FQ^2/(8\alpha_p M^{5/2})$, we have $\Gamma^* = \beta_g\theta_m\Gamma$.

As discussed in ESH15, the measurements revealed a small but significant flow in the ambient, caused by i) the diffusion of heat from the warm-air plume source along the horizontal rigid wooden base plate within which the plume nozzle was mounted, giving rise to vertical convective motion; and ii) the seeding of the ambient with a stage smoke generator. Indeed, the background mean motion, whose vertical velocity we denote Δw, was clearly captured by Particle Image Velocimetry (PIV) fields when measuring velocities away from the plume perimeter in the lower regions of the domain – a region where the plume width was significantly smaller than the lateral extent of the PIV field. Measurements indicated $\Delta w \approx 0.15$ ms^{-1} close to the source (whose radius is denoted r_0) for the jet-like, the forced and the pure-plume experiments, referred to as J, F and P, respectively. However, at larger vertical distances above the source, the size of the PIV field did not permit measurement of the (now significantly wider) plume or the ambient far beyond the plume perimeter. In ESH15 it was therefore assumed that the background motion was uniform throughout the domain; hence $\Delta w = 0.15$ ms^{-1} was subtracted from the mean vertical velocities before fitting the radial profiles with a Gaussian curve of the form

$$\frac{\overline{w}(r,z)}{w_g(z)} = \exp\left(\frac{-r^2}{r_g^2(z)}\right), \tag{A3}$$

where $w_g = 2w_m$ denotes the plume centreline velocity and $r_g = r_m/\sqrt{2}$ the Gaussian plume radius.

Figs 14(a,c,e) show the J, F and P estimates for α from ESH15 in the current notation. Indicated with the dashed line in Figs 14(a,c) is an estimate for α inferred from $r_m(z)$ (using the relations for r_m in Table II). All three estimates of α should formally provide the same value for α. For the DNS data, this is clearly the case (Fig. 10), but experiments are much more difficult to control, particularly the boundary conditions. The measurement data show a large discrepancy between the Q-based estimate for α and the one obtained from the entrainment relation (A2). This difference points to a mismatch in either the momentum balance or the mean kinetic energy balance, which can be traced back to the background flow in the ambient.

In what follows we show that the differences between our estimates for α can be significantly reduced by using a background motion whose magnitude is progressively reduced with distance from the source. As a consequence of the convection above the base plate, the plumes studied developed in a weak background velocity field that we would expect to scale as $\Delta w \sim z^{-1/3}$, i.e. the plume effectively developed within a weaker plume rising from the base plate. By applying a background correction of the form $\Delta w = 0.15(z/z_0)^{-1/3}$ where z_0 is the distance from the plate where the ambient vertical velocity was 0.15 m/s, the three estimates of α exhibit an improved agreement, as shown in Figs 14(b,d,f); all estimates are in reasonably good agreement with each other.

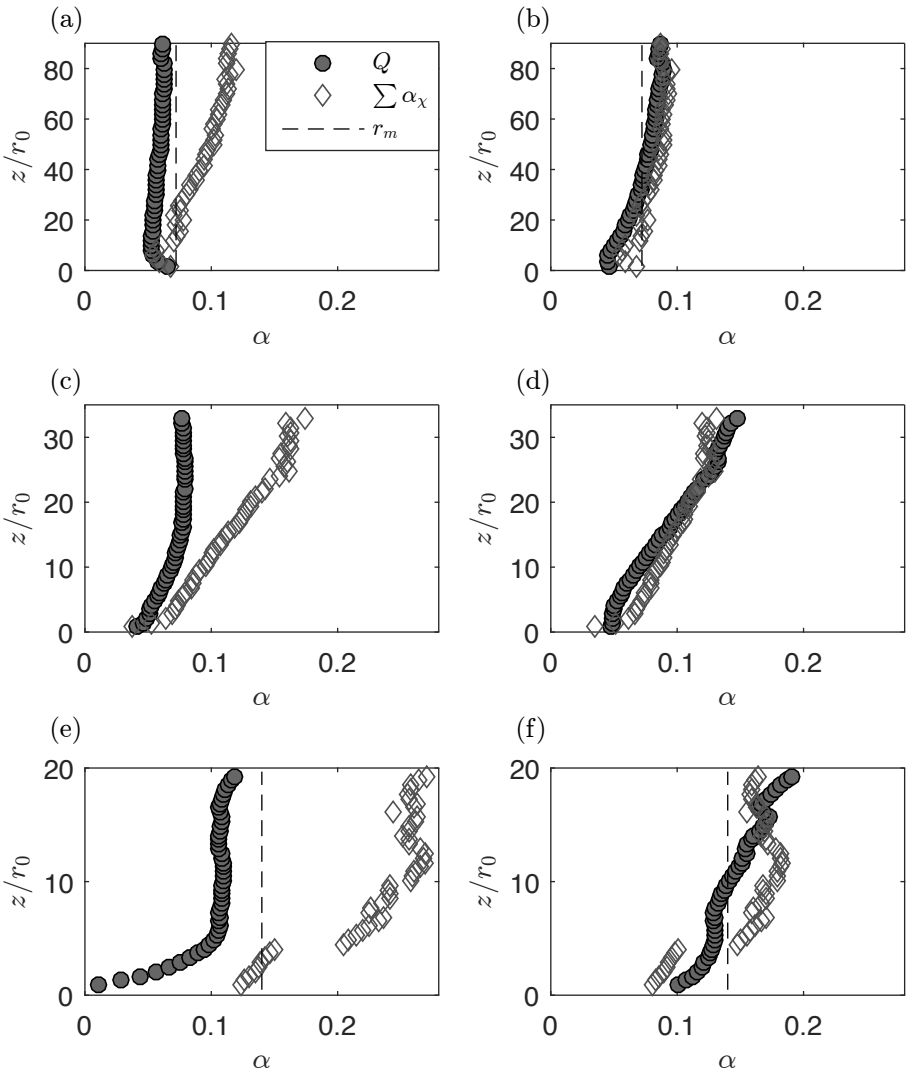

FIG. 14. Variation of entrainment coefficient as a function of distance above the source. Comparison of entrainment coefficient estimated from r_m, the volume flux balance (6) and from the entrainment relation (A2) for J (a,b), F (c,d), P (e,f). (a,c,e) $\Delta w = 0.15$ ms^{-1}. (b,d,f) $\Delta w = 0.15(z/z_0)^{-1/3}$ ms^{-1}.

The method by which δ_m has been calculated for the entrainment relation data (A2) is performed differently than in ESH15. Indeed, upon close inspection of the experimental radial profiles of the Reynolds stress $\overline{u'w'}$, in ESH15 the gradient diffusion hypothesis led to a systematic overestimation of δ_m. As in ESH15, the $\overline{u'w'}$ profile is fitted to a function of the form

$$\frac{\overline{u'w'}}{w_g^2} = 2\langle\widehat{\nu_T}\rangle \frac{r}{r_g} \exp\left(-\frac{r^2}{r_g^2}\right), \tag{A4}$$

which follows from the substituting the Gaussian velocity profile (A3) into the gradient-diffusion hypothesis (24) using a constant (in r) eddy viscosity $\langle\nu_T\rangle = w_g r_g \langle\widehat{\nu_T}\rangle$. However, we now consider r_g as a free parameter (not necessarily fixed by the value provided by the fit of (A3)), and calculate $\langle\widehat{\nu_T}\rangle$ based on the value of r_g for which the least-squares error between the measurements and (A4) is minimised.

By substituting (A3), (A4) into the definition for δ_m, it immediately follows that $\delta_m = -8\sqrt{2}\langle\widehat{\nu_T}\rangle$; the corrected values for both $\langle\widehat{\nu_T}\rangle$ and δ_m are shown in Fig. 15(b). For all three releases, the values for δ_m are now reasonably consistent, although there is a clear increasing trend with z that is not consistent with fully self-similar behaviour (in which case δ_m is expected to be constant). Nevertheless, the data is much more consistent than the original ambient-flow correction estimate shown in Fig. 15(a). The data shown in Figs 14(b,d,f) and 15(b) was used to provide the input to Table 3 in van Reeuwijk and Craske[26].

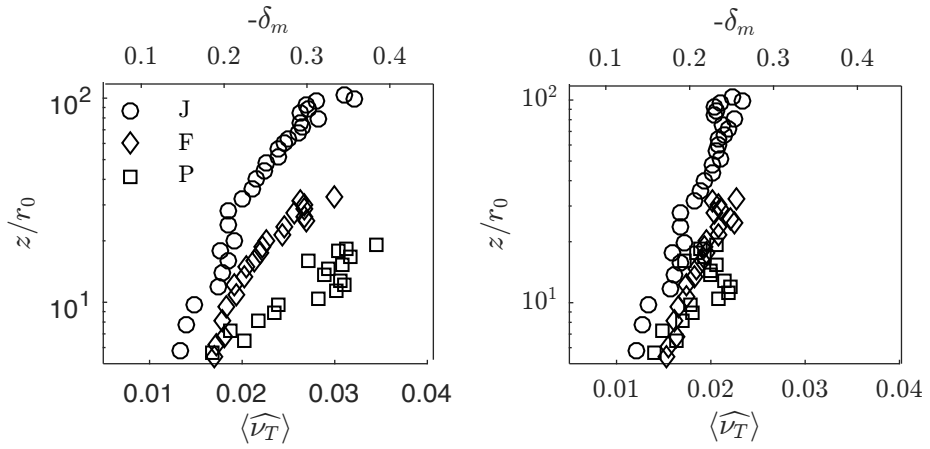

FIG. 15. Vertical evolution of δ_m for J, F and P. (a) $\Delta w = 0.15$ ms^{-1}. (b) $\Delta w = 0.15(z/z_0)^{-1/3}$ ms^{-1}.

[1] J. C. R. Hunt, "Industrial and environmental fluid mechanics," Annu. Rev. Fluid Mech. **23**, 1–41 (1991).
[2] Y. Zel'dovich, "The asymptotic laws of freely-ascending convective flows," Zhur. Eksper. Teor. Fiz **7**, 1463–1465 (1937).
[3] C. Priestley and F. K. Ball, "Continuous convection from an isolated source of heat," Q. J. R. Meteorol. Soc. **81**, 144–157 (1955).
[4] B. R. Morton, G. I. Taylor, and J. S. Turner, "Turbulent gravitational convection from maintained and instantaneous sources," Proc. Roy. Soc. London A **234**, 1–23 (1956).
[5] B. R. Morton, "Forced plumes," J. Fluid Mech. **5**, 151–163 (1959).
[6] P. N. Papanicolaou and E. J. List, "Investigations of round vertical turbulent buoyant jets," J. Fluid Mech. **195**, 341–391 (1988).
[7] N. R. Panchapakesan and J. L. Lumley, "Turbulence measurements in axisymmetric jets of air and helium. Part 1. air jet," J. Fluid Mech. **246**, 197–224 (1993).
[8] A. Shabbir and W. K. George, "Experiments in a round turbulent buoyant plume," J. Fluid Mech. **275**, 1–32 (1994).
[9] H. Wang and A. W.-K. Law, "Second-order integral model for a round turbulent buoyant jet," J. Fluid Mech. **459**, 397–428 (2002).
[10] M. V. Pham, F. Plourde, and K. S. Doan, "Direct and large-eddy simulations of a pure thermal plume," Phys. Fluids **19**, 125103 (2007).
[11] F. Plourde, M. V. Pham, S. D. Kim, and S. Balachandar, "Direct numerical simulations of a rapidly expanding thermal plume: structure and entrainment interaction," J. Fluid Mech. **604**, 99–123 (2008).
[12] E. List, "Turbulent jets and plumes," Annu. Rev. Fluid Mech. **14**, 189–212 (1982).
[13] A. W. Woods, "Turbulent plumes in nature," Annu. Rev. Fluid Mech. **42**, 391–412 (2010).
[14] G. R. Hunt and T. S. van den Bremer, "Classical plume theory: 1937-2010 and beyond," IMA J. App. Math. **76**, 424–448 (2011).
[15] G. R. Hunt and N. B. Kaye, "Lazy plumes," J. Fluid Mech. **533**, 329–338 (2005).
[16] J. Craske, A. Debugne, and M. van Reeuwijk, "Shear-flow dispersion in turbulent jets," J. Fluid Mech. **781**, 28–51. (2015).
[17] E. Kaminski, S. Tait, and G. Carazzo, "Turbulent entrainment in jets with arbitrary buoyancy," J. Fluid Mech. **526**, 361–376 (2005).
[18] G. I. Taylor, "Dynamics of a mass of hot gas rising in air." Tech. Rep. (U.S. Atomic Energy Commission. Los Alamos National Laboratory Research Library. Report 236, 1945).
[19] G. K. Batchelor, "Heat convection and buoyancy effects in fluids." Quart. J. Roy. Met. Soc. **80**, 339–358 (1954).
[20] J. Turner, "Turbulent entrainment: the development of the entrainment assumption, and its application to geophysical flows," J. Fluid Mech. **173**, 431–471 (1986).
[21] G. Carazzo, E. Kaminski, and S. Tait, "The route to self-similarity in turbulent jets and plumes," J. Fluid Mech. **547**, 137–148 (2006).
[22] E. J. List and J. Imberger, "Turbulent entrainment in buoyant jets and plumes," J. Hydraul. Div. ASCE **99**, 1461–1474. (1973).
[23] H. B. Fischer, E. J. List, R. C. Koh, J. Imberger, and N. H. Brooks, *Mixing in Inland and Coastal Waters* (Academic Press, 1979).
[24] D. G. Fox, "Forced plume in a stratified fluid," J. Geophys. Res. **75**, 6818–6835 (1970).
[25] A. Ezzamel, P. Salizzoni, and G. R. Hunt, "Dynamical variability of axisymmetric buoyant plumes," J. Fluid Mech. **765**, 576—611 (2015).
[26] M. van Reeuwijk and J. Craske, "Energy-consistent entrainment relations for jets and plumes," J. Fluid Mech. **782**, 333 – 355 (2015).
[27] C. Chen and W. Rodi, *Vertical turbulent buoyant jets - a review of experimental data* (Pergamon Press, 1980).
[28] L. P. Chua and R. A. Antonia, "Turbulent Prandtl number in a circular jet," Int. J. Heat Mass Trans. **33**, 331–339 (1990).
[29] G. R. Hunt and N. B. Kaye, "Virtual origin correction for lazy turbulent plumes," J. Fluid Mech. **435**, 377–396 (2001).
[30] W. K. George, R. Alpert, and F. Tamanini, "Turbulence measurements in an axisymmetric buoyant plume," Int. J. Heat and Mass Transfer **20**, 1145–1154 (1977).

[31]H. Rouse, C. S. Yih, and H. W. Humphreys, "Gravitational convection from a boundary source," Tellus **4**, 201–210 (1952).
[32]B. J. Devenish, G. G. Rooney, and D. J. Thomson, "Large-eddy simulation of a buoyant plume in uniform and stably stratified environments," J. Fluid Mech. **652**, 75–103 (2010).
[33]J. Craske and M. van Reeuwijk, "Energy dispersion in turbulent jets. Part 1. Direct simulation of steady and unsteady jets," J. Fluid Mech. **763**, 500 – 537 (2015).
[34]J. Craske and M. van Reeuwijk, "Robust and accurate open boundary conditions for incompressible turbulent jets and plumes," Comp. Fluids **86**, 284–297 (2013).
[35]J. Craske and M. van Reeuwijk, "Energy dispersion in turbulent jets. Part 2. A robust model for unsteady jets," J. Fluid Mech. **763**, 538 – 566 (2015).
[36]J. Craske and M. van Reeuwijk, "Generalised unsteady plume theory," Journal of Fluid Mechanics **792**, 1013–1052 (2016).
[37]J. H. Hussein, S. P. Capp, and W. K. George, "Velocity measurements in a high-Reynolds-number, momentum conserving, axisymetric jet," J. Fluid Mech. **258**, 31–75 (1994).
[38]S. B. Pope, *Turbulent Flows* (Cambridge University Press, 2000).
[39]F. Kuznik, G. Rusaouen, and J. Brau, "Experimental study of turbulent structures in a non isothermal horizontal jet issuing from a round nozzle distanced from a wall," Int. J. Ventil. **10** (2011).
[40]M. Woodhouse, J. Phillips, and A. Hogg, "Unsteady turbulent buoyant plumes." J. Fluid Mech. **794,**, 595–638. (2016).
[41]P. Linden, "Perspectives in fluid dynamics, a collective introduction to current research," (Cambridge University Press, 2003) Chap. Convection in the Environment, pp. 289–346.
[42]H. Schlichting, *Boundary layer theory* (McGraw-Hill, 1960).
[43]J. Chen and E. J. List, "Spreading of buoyant discharges," in *Proc. 1976 ICHMT seminar on turbulent buoyant convection* (1976) pp. 171–182.